Fast Resonance Frequency Optical Modulation in Superconducting Stripline Resonator

Eran Arbel-Segev, Baleegh Abdo, *Student Member, IEEE*, Oleg Shtempluck, and Eyal Buks

***Abstract*—Fast resonance frequency optical modulation of a superconducting stripline resonator is investigated. The experiments are performed using a novel device which integrates a hot electron detector (HED) into a superconducting stripline ring resonator. Frequency modulation is demonstrated by both applying dc current or voltage to the HED, and by applying optical illumination, with modulation frequencies of up to 4.2 GHz. Potential applications for such a device are in telecommunication, quantum cryptography, and biofluorescence.**

***Index Terms*—Hot-electron detector, NbN, optical modulation, parametric excitation, superconducting ring resonator.**

I. Introduction

RESONANCE parametric amplifiers are characterized by very low noise, high gain, and phase sensitive amplification. Parametric resonance in superconducting resonators [1] may allow some intriguing applications such as quantum squeezing [2], quantum nondemolition measurements [3], photon creation by the so-called dynamical Casimir effect [4], and more.

Parametric excitation occurs when the resonance frequency of an oscillator varies in time. The first parametric resonance occurs when the excitation is performed periodically at twice the resonance frequency f_0, namely $f(t) = f_0[1 + \xi \cos(4\pi f_0 t)]$ [5]. The system's response to such an excitation depends on the dimensionless parameter ξQ, where Q is the quality factor of the resonator. When $\xi Q < 1$, the system is said to be in the subthreshold region, while above threshold, when $\xi Q > 1$, the system breaks into oscillation. Achieving parametric gain where $\xi Q > 1$ requires that the shift in the resonance frequency exceeds the width of its peak [6].

The frequency modulation mechanism we employ here is based on changing the boundary conditions of a superconducting resonator. This is done by switching a small section of the resonator to a normal state by using optical illumination. The switching time in superconductors is usually limited by the relaxation process of high-energy quasi-particles, also called "hot-electrons," giving their energy to the lattice, and recombining to form Cooper pairs. Recent experiments with photodetectors, based on a thin layer of superconducting niobium–nitride (NbN), have demonstrated an intrinsic switching time on the order of 30 ps and a counting rate exceeding 2 GHz (see [7] and references therein). Resonance frequency shift by optical radiation [8]–[10], or high-energy particles [11], [12] (for which the required condition $\xi Q \cong 1$ has been achieved) was demonstrated, though no periodic modulation was reported. Resonance frequency tuning [13] and switching [14] as well as optical and microwave signal mixing [15], [16] were demonstrated in normal-conducting GaAs microstrip ring resonators.

In this paper, we show experimentally that resonance frequency modulation, at twice the resonance frequency, is within reach using superconducting microwave resonators. Furthermore, the parametric gain threshold conditions, namely $\xi Q > 1$, is demonstrated in a continuous-wave (CW) measurement. The experiments are performed using a novel device, that integrates a hot electron detector (HED) into a superconducting ring resonator. The HED is used as an optically tuned, lumped element, that changes the boundary conditions of the resonator [17], and thus manipulates its resonance frequencies.

In Section II, we describe the circuit design and fabrication process. Section III starts with the HED response to applied dc voltage and current, and the resulting effect on the resonance frequencies. These results are followed by a comparison with a theoretical model. Afterwards, the effect of CW and modulated infrared (IR) light on the resonance frequency is described, and fast optical modulation of the resonance frequency is demonstrated.

II. Circuit Design and Fabrication

A. Circuit Design

The circuit layout is illustrated in Fig. 1(a). The device is made of 8-nm-thick NbN stripline, fabricated on a sapphire wafer, with dimensions of $34 \times 30 \times 1$ mm^3. The design integrates three components. The first is a superconducting ring resonator, having a radius of 6.39 mm, and its feedline. Ring configuration is a symmetric and compact geometry, which is generally suitable for applications, which require resonance tuning [13]. The first few resonance frequencies are designed for the S- and C-bands (2–8 GHz). The resonator is weakly coupled to its feedline, where the coupling gap is 0.4 mm. The stripline width is set to 347 μm to obtain a characteristic impedance of $Z_0 = 50\ \Omega$.

The second component is an HED, which is monolithically integrated into the ring structure. Its angular location, relative to the feedline coupling location, maximizes the RF current amplitude flowing through it, and thus maximizes its coupling to the

Manuscript received January 10, 2006; revised March 7, 2006. This paper was recommended by Associate Editor M. Mueck. This work was supported by MAFAT, Israel Science Foundation under Grant 1380021, by the Deborah Foundation, and by the Poznanski Foundation.

The authors are with the Department of Electrical Engineering and Microelectronics Research Center, Technion, Haifa 32000, Israel (e-mail: segeve@tx.technion.ac.il).

Color versions of Figs. 2–11 are available online at http://ieeexplore.ieee.org.
Digital Object Identifier 10.1109/TASC.2006.874961

1051-8223/$20.00 © 2006 IEEE

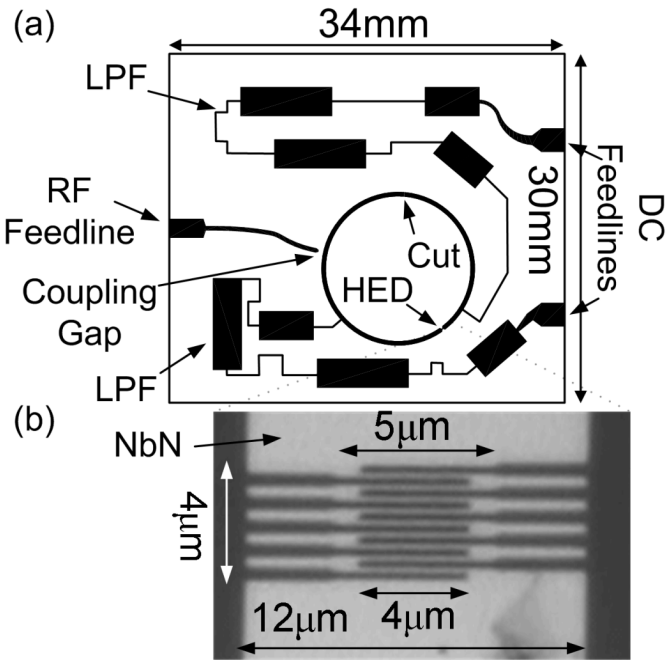

Fig. 1. (a) Device layout. (b) Optical microscope image of the HED.

resonator. The HED, shown in Fig. 1(b), has a 4×4 μm^2 meander structure and consists of nine NbN superconducting strips. Each strip has a characteristic area of 0.15×4 μm^2 and the strips are separated one from another by approximately 0.25 μm [18].

The HED operating point is maintained by applying dc bias. The dc bias lines, forming the third component, are designed as two superconducting on-chip low-pass filters (LPF) with a cutoff frequency of 1.2 GHz. As this frequency is lower than the fundamental resonance frequency of the resonator, the intrinsic fields of the resonator are not appreciably perturbed. A cut of 20 μm is made in the perimeter of the resonator to force the dc bias current flow through the HED.

The device, which is top covered by a bare sapphire substrate, is housed in a gold-plated Faraday package made of oxygen-free high conductivity copper. Superconducting niobium ground planes are dc-magnetron sputtered on the inner covers of the package. RF power is fed using an SMA launcher, coupled to the feedline. A dc bias is fed through two π-LPFs, screwed to the package, having a cutoff frequency of 1 MHz. IR laser light is guided to the device by a fiber-optic cable. A through hole of 1 mm in diameter is drilled in the Faraday package, and a fiber-optic connector affixes the tip of the fiber cable at approximately 9.55 mm above the HED.

B. Fabrication Process

The fabrication process starts with a thorough precleaning of the sapphire wafer in solvents. We have experienced that the commonly employed process of piranha followed by RCA cleaning substantially reduces the NbN adhesion to the sapphire wafer. In the next step, 200-nm-thick gold pads are thermally evaporated through a mechanical mask to form the dc contact pads. The mask partially shadows the evaporation and, thus, the pads' perimeters are smoothed. Epitaxy 8-nm-thick NbN film is then deposited at 700 °C using a dc-magnetron sputtering system [19]. Sputtering parameters are summarized in Table I and the process itself is further detailed in [20]. Next, an aluminum–nitride (AlN) layer of 7 nm thickness is *in-situ* sputtered in N_2 atmosphere at a temperature lower than 100 °C. This layer protects the vulnerable NbN layer during the following fabrication processes and restrain degradation [21]. It also has a functional role, as at cryogenic temperatures, it serves as a thermal conducting layer, which enhances the cooling of the NbN layer. In the next step, the HED meander stripline is patterned using electron beam lithography (EBL). The deposition of an 80-nm-thick PMMA 950K layer is followed by EBL with the following parameters: 40 kV, 15 pA, and 2.1 nC/cm, corresponding to acceleration voltage, emission current, and line dose, respectively. Afterwards, the AlN layer is directly etched through the PMMA mask using ion milling. The remaining AlN layer serves as a mask for the sequential etching of the NbN layer, using low-power reactive ion etching (RIE) in the SF_6 environment [22]. The remaining PMMA is removed by NMP. The last fabrication step is the patterning of the resonator and the LPFs features. This is achieved by using the standard photolithography process. The photoresist development process (employing AZ-326 photoresist developer) also wet etches the AlN layer [23], while the remaining layer is again used as a mask for the RIE etching of the NbN film.

TABLE I
SPUTTERING PARAMETERS

Process parameter	NbN	AlN
Partial flow ratios (Ar,N_2)	(87.5%,12.5%)	(0%,100%)
Base temperature	700 °C	60 °C
Base pressure	$3.6 \cdot 10^{-7}$ torr	$1.8 \cdot 10^{-7}$ torr
Work pressure	$6.8 \cdot 10^{-3}$ torr	$2.9 \cdot 10^{-3}$ torr
Discharge current	360mA	360mA
Discharge voltage	311V	292V
Deposition rate	3.6 Å/sec	1.1 Å/sec
Thickness (t)	8nm	7nm
Target-substrate distance	95mm	230mm

III. EXPERIMENTAL AND NUMERICAL RESULTS

All measurements presented in this paper are carried out in a fully immersed sample in liquid helium (4.2 K). The experimental setup, used for reflection measurements, is schematically depicted in Fig. 2. The sample's RF feedline is connected to a vector network analyzer using a semirigid coax cable. The dc feedlines are connected to a dc source-measure unit using four-probe wiring. The laser source has a wavelength of 1550 nm.

A. DC I–V Measurements

The basic current–voltage (*I–V*) characteristics of the HED meander stripline, shown in Fig. 3, exhibit a highly complex hysteretic behavior. Panel 3(a) plots nine current measurements, obtained while increasing the applied voltage (solid blue), one on top of the other, where each measurement starts at zero voltage and ends at a different maximum voltage, slightly above the voltages V_{Cn}, depicted in the figure. The corresponding nine current measurements, obtained while

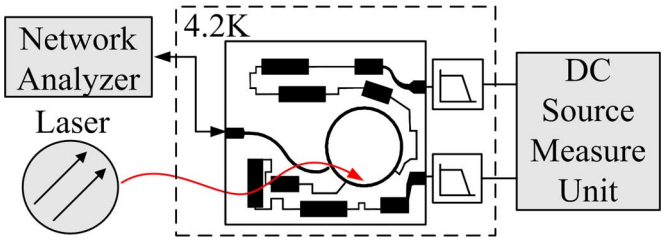

Fig. 2. Setup used for reflection measurements.

decreasing the applied voltage are also plotted (dashed–dotted red). The dashed magenta and dotted black correspond to similar measurements, taken while the HED is being illuminated. The measurements for low applied voltages and currents are enlarged in the insets of Fig. 3(a) and (b), respectively, where the finite resistance, of approximately 300 Ω, is due to the contacts.

In Fig. 3(a), eight clearly distinguished abrupt jumps in the measured current are noticed. In addition, looking at the insets, one identifies another small current jump. The number of current jumps corresponds to the number of stripline sections that compose the meander shape of the HED. Each jump, except for the first one, is the result of a large increase in the HED resistance due to a transition of one section from the superconducting state to the normal one. The first jump has a rather small amplitude due to the serial contact resistance. In addition, the first jump occurs at the most nonuniform stripline section, which, thus fragmentally shifts to the normal state, and thus the increase in the resistance spreads over a rather large voltage range, starting at V_{C1} and ending at approximately 40 mV.

Resistance jump is typical for a superconducting microbridge and is caused by the formation of a hotspot in the bridge area [24]. Each critical voltage V_{Cn} varies, in general, between different scans, indicating thus, the stochastic nature of the transitions between bistable states. The fluctuation ΔV_{Cn} in V_{Cn} between different scans characterizes the lifetime of the prejump metastable states of the system. The increase in ΔV_{Cn} at high voltages indicates a decrease in the lifetime of metastable states because of larger temperature fluctuations. The combined results of the increasing and decreasing applied voltage measurements show that large hysteresis is present at all current jumps except for the first one. This observation indicates, that only one section at a time can be biased into subcritical conditions. Furthermore, only the section responsible for the first jump, at V_{C1}, does not suffer form hysteresis and, thus, can repetitively respond to radiation. Probably the cause for this discretization of the critical current is the nonuniformity in the meander shape of the HED [24], [25]. Our finding clearly shows that the nonuniformity may substantially reduce the effective area of the HED, up to a fraction of one ninth of its printed area in the present design.

The same measurements are repeated while constantly illuminating the HED with approximately 27-nW IR laser. In these measurements, the current jumps occur at lower applied voltages $V'_{Cn} < V_{Cn}$. In addition, ΔV_{Cn} are substantially widened. The decrease in the critical voltage values can be explained by local heating of bolometric nature, due to the IR illumination.

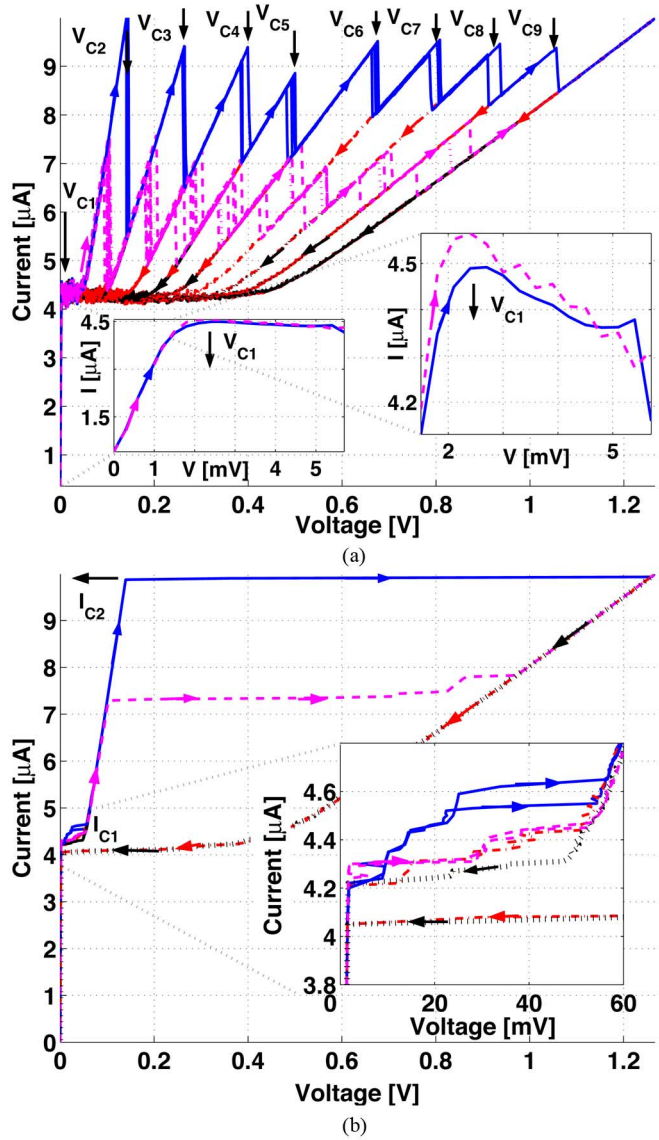

Fig. 3. Basic *I–V* characteristic of the HED meander stripline. (a) Current versus voltage and (b) voltage versus current measurements. The dashed magenta (solid blue) curves show an increasing applied voltage and current measurement, with (without) laser illumination. The dotted black (dashed–dotted red) curves show a decreasing applied voltage and current measurement, with (without) laser illumination. The insets of (a) and (b) magnify the results for small applied voltages and currents, respectively.

Fig. 3(b) shows voltage measurements, obtained while increasing the applied current, with (dashed magenta) and without (solid blue) IR illumination, and while decreasing the applied current, with (dotted black) and without (dashed–dotted red) IR illumination. One fragmented and one abrupt voltage jumps occur at distinguishable critical currents of $I_{C1} \cong 4.2\ \mu\text{A} - 4.6\ \mu\text{A}$ and $I_{C2} \cong 9.8\ \mu\text{A}$, respectively. Again, the fragmentation of the first critical current is caused by the nonuniformity of the first section that shifts to the normal state. IR illumination has a negligible measured effect on I_{C1} and a strong effect on I_{C2} values. All voltage jumps suffer from hysteresis and, therefore, current bias is an unsuitable method for repetitive radiation detection.

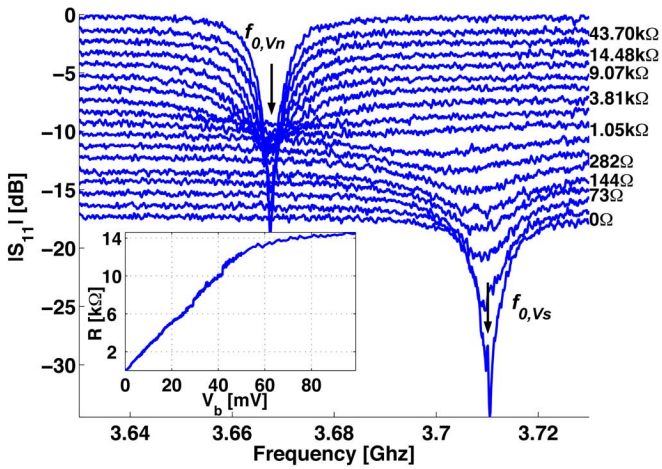

Fig. 4. Several $|S_{11}|$ measurements of the second resonance mode, as a function of frequency, for various HED resistance values. The measurements are obtained while applying variable voltage and the HED resistance is measured using the four-probe technique. Plots are shifted vertically for clarity. The inset shows the resistance versus voltage characteristics of the HED.

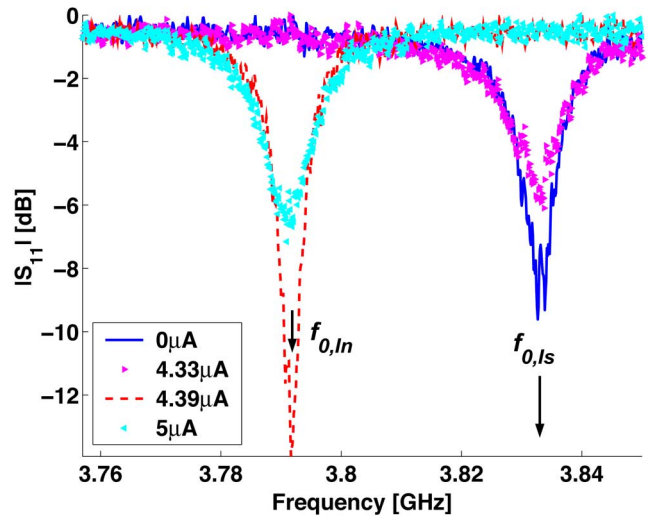

Fig. 5. Several $|S_{11}|$ measurements of the second resonance mode, as a function of frequency. The measurements are obtained while applying variable current.

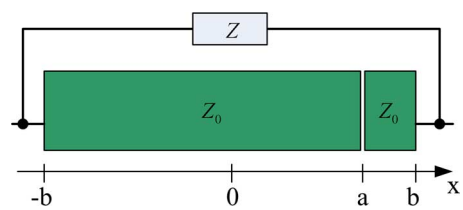

Fig. 6. Resonator model.

B. DC I–V Effect on the Resonance Lineshape

Fig. 4 shows several $|S_{11}|$ measurements as a function of frequency, in the vicinity of the second resonance mode, for various HED resistance values. For clarity, the resonance curves are vertically shifted upwards, for increasing resistance values. The measurements are obtained while applying variable voltage V_b, and the resistance is measured simultaneously with the $|S_{11}|$ data using the standard four-probe technique. The RF input power is set to -64.7 dBm, where the resonator is in the linear region [26]. The inset of Fig. 4 plots the measured HED resistance as a function of V_b.

The dependence of the resonance characteristics on the HED resistance R_{HED} can be described as follows. At zero applied voltage, the resonance frequency is $f_{0,Vs} \cong 3.71$ GHz. At very low voltages, as the HED is biased far below critical conditions, its resistance is negligible and its influence on the resonance curve as well. As the resistance increases, the resonance frequency slightly red shifts, and more important, the Q-factor is significantly reduced due to dissipation in the HED. This behavior continues up to a point, at $R_{\mathrm{HED}} \cong 1$ kΩ, where the resonance curve can be hardly detected. When increasing the resistance beyond that point, the trend of the Q-factor changes, the dissipation decreases, and the resonance curve re-emerges at a new resonance frequency $f_{0,Vn} \cong 3.665$ GHz, red shifted by approximately 45 MHz relative to its original value. The new resonance Q-factor has a value similar to the original one. When further increasing the resistance, the trend of the Q-factor continues but no additional resonance shift occurs. The behavior of the Q-factor suggests that as R_{HED} increases, the RF current amplitude of the resonance mode in the HED is reduced, due to current redistribution, and thus the total power dissipation decreases.

Similar behavior, with one major exception, can be observed under applied current, as shown in Fig. 5. The solid blue, triangle right magenta, dashed red, and triangle left cyan curves are taken with subcritical 0 μA, 4.33 μA $< I_{C1}$, and over critical 4.39 μA, 5 μA $> I_{C1}$ applied currents, respectively, where I_{C1} is the current at which a first jump in the measured voltage occurs. There are two well-defined resonance frequencies, $f_{0,Is} = 3.83$ GHz and $f_{0,In} = 3.79$ GHz, which corresponds to applied currents below and above I_{C1}, respectively. $f_{0,Is}$ and $f_{0,In}$ slightly differ from $f_{0,Vs}$ and $f_{0,Vn}$ as the two measurements were taken at different thermal cooldown cycles. Low Q-factor curves are absent from this measurement because under applied current, the HED cannot be biased into intermediate resistance values. At bias currents below I_{C1}, the HED has low resistance, which only slightly increases as the current approaches I_{C1}. As a result, no resonance shift occurs, and only the Q-factor slightly reduces as the current increases. This behavior changes abruptly once the HED resistance crosses a rather low critical value R_C. A self-sustained hotspot is generated [24], quickly expends, and the HED becomes resistive. I_{C1} is the bias current at which $R_{\mathrm{HED}} = R_C$ is obtained. This thermal runaway causes an abrupt red shift of $\Delta f_0 \cong 40$ MHz in the resonance frequency. Further increase of the bias current beyond I_{C1} increases the power dissipation and heat generation in the HED. This increases the local temperature and dissipation near the HED, and thus causes Q-factor reduction.

C. Resonance Frequency Shift Modeling

To account for our results, we calculate the resonance characteristics of our device as a function of HED resistance.

As shown in Fig. 6, the ring resonator is modeled as a straight transmission line, extending in the $\pm x$ directions. The HED is represented by a lumped discontinuity $Z = R + jwL$ connecting

TABLE II
RESONANCE FREQUENCY CHARACTERISTICS

	Numerical Results			Experimental Results		
n	f_0 [GHz] $\Delta R = 0$	f_0 [GHz] $\Delta R \to \infty$	Δf_0 [MHz]	f_0 [GHz] $\Delta R = 0$	f_0 [GHz] $\Delta R \to \infty$	Δf_0 [MHz]
1	1.913	1.873	39.8	1.59	1.58	10
2	3.791	3.747	43.7	3.874, 3.711	3.829, 3.668	45, 43
3	5.654	5.62	34.1	5.634, 5.38	5.608, 5.35	26, 30

$x = \pm b$ points together, where R is the resistance, ω is the angular frequency, and L is the total inductance of the meander shape of the HED. The transmission line has a cut at point $x = a$. The couplings to the RF and dc feedlines are neglected.

The voltage along the resonator's transmission line is given by a standing waves expression of the form [27]

$$V(x) = \begin{cases} A\cos(\beta x) + B\sin(\beta x), & -b < x < a \\ C\cos\beta(x-a) + D\sin\beta(x-a), & a < x < b \end{cases}$$

where $\beta = 2\pi f\sqrt{\epsilon_r}/c$ is the propagation constant along the transmission line, f is the frequency, ϵ_r is the relative dielectric constant, and c is the speed of light in vacuum.

The current is given by $I(x) = (i/\beta Z_0)dV/dx$, where Z_0 is the characteristic impedance of the line. By applying the boundary conditions 1) $I(a_-) = I(a_+) = 0$, 2) $I(-b) = I(b)$, and 3) $V(b) - V(-b) = I(b)Z$, we easily derive a boundary condition equation which yields the complex resonance frequencies of the resonator.

A phase transition of Z from superconducting to normal state simultaneously causes changes in its resistive $\Delta R > 0$ and inductive $\Delta L > 0$ parts. Both changes contribute to a resonance shift in the same direction. For very thin superconducting films, $\Delta R \gg \omega\Delta L$ resulting in $\Delta Z \cong \Delta R$. Three fitting parameters are used in the model. Best fit results are obtained for $R = 0\Omega$, $Z_0 = 55\ \Omega$, and $\omega L = 14.5 Z_0$, which leads to $L = 37.3$ nH for the second resonance mode. $R \ll Z_0$ in the superconducting state, and thus negligible. The characteristic impedance Z_0 value is in a very good agreement with the designed value of 50 Ω. The calculated inductance L of the meander line at 4.2 K without any applied current is 6.05 nH [28], but this value is strongly dependent on temperature and current density [28], [29], so the fit parameter value is in reasonable agreement with the calculated one.

Table II summarizes the first three solutions of the boundary condition equation for the two extreme cases of $\Delta R = 0$ and $\Delta R \to \infty$. Comparing these results to the measured results (taken at two different cooldown cycles), also summarized in Table II, shows a good agreement, especially for the second and third modes, for which the resonator is designed.

Fig. 7 shows the second resonance characteristics, resonance frequency, and unloaded damping rate γ_2 [2], of the experimental data (solid blue) and the numerically calculated data (dashed red). The rate γ_2 is extracted from the data plotted in Fig. 4 using the method presented in the Appendix. The upper subplot shows the resonance frequency as a function of ΔR. The calculated resonance frequency, at zero resistance, is $f_0 =$

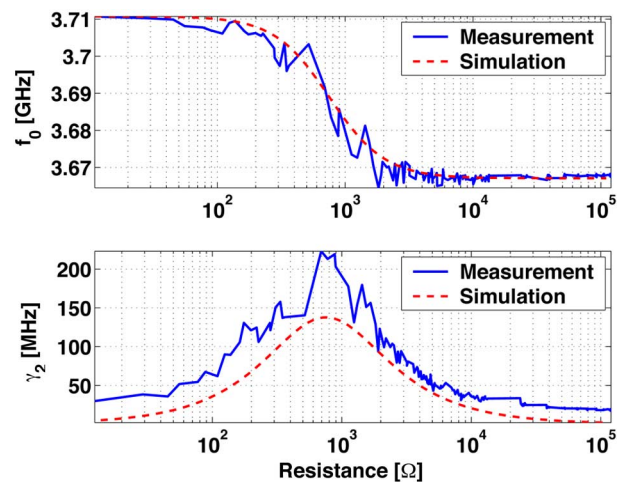

Fig. 7. Resonance frequency and unloaded damping rate γ_2 of the second resonance mode.

3.791 GHz, which equals the mean value of the resonance frequency measured at different cooldown cycles. In this subplot, the calculated data is corrected by −80 MHz to overlap between the first calculated and measured point. Both curves show the same dependence on ΔR. The lower subplot shows the unloaded damping rate γ_2, as a function of ΔR. Also in this case, a good agreement with the experiment is obtained, and as expected, the measured damping rate exceeds the calculated one, due to losses, which are not taken into account in the model.

The coupling between the different modes and the HED can be characterized by the current amplitude through the HED. The model predicts normalized current amplitudes of 7.3% and 5.7% inside the lumped element, for the second and third modes, respectively. This rather weak coupling is the result of the rather high kinetic inductance of the HED. To estimate the coupling of modes two and three to the feedline [30], we show in Fig. 8 the normalized voltage amplitudes, as a function of the ring's angular location. The calculated normalized voltage amplitudes, at the feedline coupling location, are 71% and 92%, respectively. The voltage amplitudes distribution have, in general, a strong dependence on the resonance frequency, and hence on ΔR, but because of the rather small resonance shift, the voltage amplitudes at the coupling location change by less than 2%.

D. IR Illumination Effect on the Resonance Lineshape

Fig. 9 plots $|S_{11}|$ measurements with (dashed red) and without (solid blue) IR illumination. The effective IR illumination power, impinging on the HED, is approximately 27 nW.

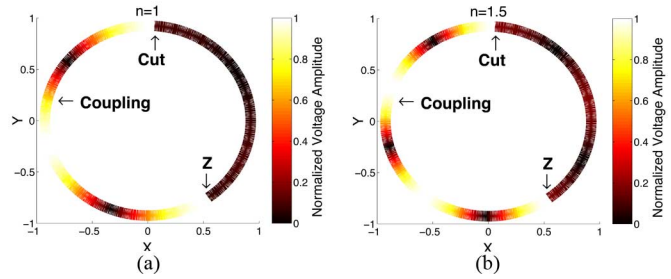

Fig. 8. Normalized voltage amplitudes as a function of the ring's angular location, for the (a) second and (b) third resonance modes.

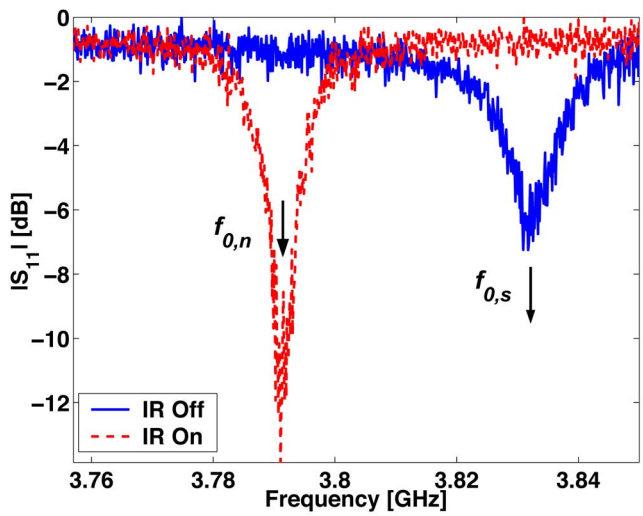

Fig. 9. Several $|S_{11}|$ measurements of the second resonance mode, as a function of frequency, while applying subcritical current, with (dashed red) and without (solid blue) IR illumination.

The RF input power is set to −64.7 dBm and the HED is biased with a subcritical dc current of 4.14 μA, which only weakly influences the resonance curve. When the illumination is turned on, the resonance frequency abruptly shifts to a lower frequency. The new resonance lineshape has the same characteristics as the resonance lineshape measured without illumination under supercritical bias current of $I = 4.39\,\mu\text{A} > I_{C1}$. This measurement clearly shows that the resonance frequency is sensitive to IR illumination. The measured results in this experiment yield $\xi Q \cong 4.14$.

E. Fast Modulation of the Resonance Frequency

Fast modulation of the resonance frequency is performed using the experimental setup depicted in Fig. 10. The resonator is excited by a CW pump signal, at frequency $f_0 = 3.71$ GHz, which coincides with the second resonance frequency. The optical signal is modulated at frequency Δf, using a Mach–Zehnder modulator driven by a second CW signal phase locked with the first one. The reflected power is mainly composed of three tones. One is the reflected pump signal at frequency f_0. The other two are sidebands, produced by mixing the pump signal and the optical modulation signal [31], and are found at frequencies $f_{1,2} = f_0 \pm \Delta f$. Occasionally, higher

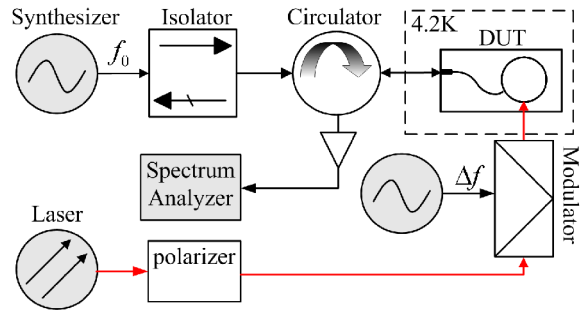

Fig. 10. Setup used for resonance frequency optical modulation.

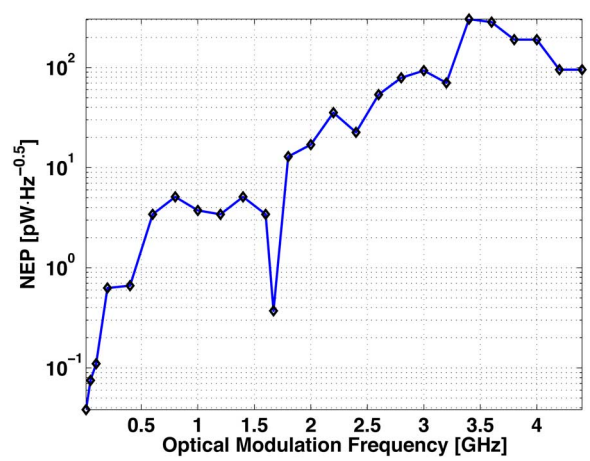

Fig. 11. NEP for various optical modulation frequencies.

orders of the mixed signals are also detected. The amplified reflected power is measured using a spectrum analyzer, which tracks the $f_1 = f_0 + \Delta f$ tone. No dc bias is needed in this measurement as the RF probe signal also serves as a bias signal for the HED. This bias scheme has two major advantages over the dc bias scheme; first the RF pump bias signal has lower noise, as the $1/f$ and line noises are avoided. Second, the RF bias signal introduces a strong nonlinear mechanism [26], [32], which will be discussed in a future publication [33], and produces a high internal gain of the induced optical signal.

The device is not designed for radiation detection. Nevertheless, we find it useful to characterize the response to optical modulation by its noise equivalent power (NEP). Fig. 11 shows the NEP of the device for various optical modulation frequencies. Each NEP data point is derived out of several reflected power measurements in the vicinity of f_1, where each measurement is performed with a different pump power, and ranges between −54.7 dBm and −45.7 dBm. The best NEP is measured for a modulation frequency of $\Delta f = 10$ MHz, and equals 38 $fW/\sqrt{\text{Hz}}$. A rather low NEP of 370 $fW/\sqrt{\text{Hz}}$ is measured for a modulation frequency of $\Delta f = 1.699$ GHz. For this modulation frequency, f_1 coincides with the third resonance frequency of the resonator. Higher modulation frequencies than the ones presented in Fig. 11 are also observed, but the measured NEP is relatively poor, mainly due to the bandwidth limitations of the microwave components composing the experimental setup.

IV. Discussion

Fast modulation of the resonance frequency is experimentally demonstrated. Furthermore, the parametric gain threshold condition is achieved in a CW measurement. The main problem, which currently prevents parametric gain to occur, is the relatively low photon flux that impinges the HED. Due to losses along the optical path, especially the expansion of the Gaussian beam from the tip of the fiber to the HED, the largest photon flux we currently manage to apply is approximately 13 photons per modulation cycle, at twice the resonance frequency. When taking into account the quantum efficiency of the HED, which is probably lower than 1% [34], [35], and its effective area, which as discussed in Section III-A is probably smaller than its printed area, we estimate that the optical power flux is one to three orders of magnitude lower than the threshold power. The uncertainty in the estimation is originated from the fact, that in the bias scheme we employ, it is hard to estimate the ratio between the current density and the critical current density in the HED. We conclude that parametric gain cannot be achieved using the present device. Future devices will address this problem.

V. Conclusion

We have reviewed the design, fabrication, and measurement results of our optically tunable resonator. Resonance frequency modulation frequency as high as 4.2 GHz is achieved, and an NEP of 38 $fW/\sqrt{\mathrm{Hz}}$ in the IR is measured. The parametric gain threshold condition is achieved in a CW measurement. Moreover, the results are shown to be in a good agreement with a theoretical modeling. The approach used in this device has a great potential of achieving a parametric amplification in superconducting resonators.

Appendix
Damping Rate Extraction

The universal expression for the reflection amplitude of a linear resonator near resonance is [2], [36]

$$S_{11} = \frac{i\Omega + (\gamma_1 - \gamma_2)}{i\Omega - (\gamma_1 + \gamma_2)} \tag{1}$$

where $\Omega = \omega_p - \omega_0$ is the pump angular frequency ω_p, relative to the angular resonance frequency ω_0, γ_1 is the coupling constant between the resonator and the feedline, and γ_2 is the unloaded damping rate of the resonance. The damping rate is numerically extracted by expanding (1) to first order in Ω

$$S_{11} = r_0 + r_1\Omega + O(\Omega^2)$$

where r_0 is the S_{11} value at the resonance frequency

$$r_0 = \frac{\gamma_2 - \gamma_1}{\gamma_1 + \gamma_2}$$

and r_1 is the slope of the imaginary part of S_{11}

$$r_1 = -i\frac{2\gamma_1}{(\gamma_1 + \gamma_2)^2}.$$

Note that the extraction of r_1 is less accurate for low Q-factor curves, and thus, the calculated loss factor suffers from a rather large impreciseness at that region.

References

[1] N. V. Fomin, O. L. Shalaevand, and D. V. Shantsev, "Parametric resonance in superconducting micron-scale waveguides," *J. Appl. Phys.*, vol. 81, no. 12, pp. 8091–8096, Jun. 1997.

[2] B. Yurke and E. Buks, "Performance of cavity-Parametric Amplifiers, Employing Kerr Nonlinearites, in the Presence of Two-Photon Loss," *arXiv:quant-ph/0505018 v1*, pp. 1–9, 2005.

[3] B. C. Sanders and G. J. Milburn, "Complementarity in a quantum nondemolition measurement," *Phys. Rev. A*, vol. 39, no. 2, pp. 694–702, Jan. 1989.

[4] V. V. Dodonov and A. B. Klimov, "Generation and detection of photons in a cavity with a resonantly oscillating boundary," *Phys. Rev. A*, vol. 53, no. 4, pp. 2664–2682, Apr. 1996.

[5] L. Landau and E. Lifshits, *Mechanics*. New York: Oxford, 1976.

[6] M. A. Golosovsky, H. J. Snortland, and M. R. Beasley, "Nonlinear microwave properties of superconducting Nb microstrip resonators," *Phys. Rev. B*, vol. 51, no. 10, pp. 6462–6469, 1995.

[7] G. N. Goltsman, A. Korneev, I. Rubtsova, I. Milostnaya, G. Chulkova, O. Minaeva, K. Smirnov, B. Voronov, W. Sysz, A. Pearlman, A. Verevkin, and R. Sobolewski, "Ultrafast superconducting single-photon detectors for near-infrared-wavelength quantum communications," *Phys. Status Solidi C*, vol. 2, no. 5, pp. 1480–1488, 2005.

[8] S. Cho and C.-S. Son, "Modulation of the resonance frequency of superconducting microwave resonators," *IEEE Trans. Appl. Superconduct.*, vol. 13, no. 2, pp. 3659–3662, Jun. 2003.

[9] ——, "Observation of bolometric optical response in superconducting microwave meander lines," *J. Appl. Phys.*, vol. 84, no. 10, pp. 5657–5661, Nov. 1998.

[10] M. Tsindlekht, M. Golosovsky, H. Chayet, and D. Davidov, "Frequency modulation of the superconducting parallel-plate microwave resonator by laser irradiation," *Appl. Phys. Lett.*, vol. 65, no. 22, pp. 2875–2877, Nov. 1994.

[11] P. K. Day, H. G. LeDuc, B. A. Mazin, A. Vayonakis, and J. Zmuidzinas, "A broadband superconducting detector suitable for use in large arrays," *Nature*, vol. 425, pp. 817–821, Oct. 2003.

[12] R. Wedenig, T. Niinikoski, P. Berglund, J. Kyynarainen, R. Inen, L. Costa, M. Valtonen, R. Linna, J. Salmi, H. SeppaK, and I. Suni, "Superconducting NbN microstrip detectors," *Nucl. Instrum. Methods Phys. Res. A*, vol. 443, no. 3, pp. 646–663, Sep. 1999.

[13] K. Chang, S. Martin, F. Wang, and J. L. Klein, "On the study of microstrip ring and varactor-tuned ring circuits," *IEEE Trans. Microw. Theory Tech.*, vol. MTT-35, no. 12, pp. 1733–1739, Dec. 1987.

[14] T. S. Martin, F. Wang, and K. Chang, "Theoretical and experimental investigation of novel varactor-tuned switchable microstrip rmg resonator circuits," *IEEE Trans. Microw. Theory Tech.*, vol. 36, no. 12, pp. 1733–1739, Dec. 1988.

[15] J.-C. Lee, H. F. Taylor, and K. Chang, "Degenerate parametric amplification in an optoelectronic GaAs CPW-to-slotline ring resonator," *IEEE Microw. Guided Wave Lett.*, vol. 7, no. 9, pp. 267–269, Sep. 1997.

[16] G. K. Gopalakrishnan, B. W. Fairchild, C. L. Yeh, C.-S. Park, K. Chang, M. H. Weichold, and H. F. Taylor, "Experimental investigation of microwave-optoelectronic interactions in a microstrip ring resonator," *IEEE Trans. Microw. Theory Tech.*, vol. 39, no. 12, pp. 2052–2060, Dec. 1991.

[17] D. Saeedkia, A. H. Majedi, S. Safavi-Naeini, and R. R. Mansour, "Frequency and time-varying scattering parameters of a photo-excited superconducting microbridge," *IEEE Microw. Wireless Compon. Lett.*, vol. 15, no. 8, pp. 510–512, Aug. 2005.

[18] J. Zhang, W. Slysz, A. Verevkin, O. Okunev, G. Chulkova, A. Korneev, A. Lipatov, G. N. Goltsman, and R. Sobolewski, "Response time characterization of NbN superconducting single-photon detectors," *IEEE Trans. Appl. Superconduct.*, vol. 13, no. 2, pp. 180–183, Jun. 2003.

[19] G. N. Goltsman, K. Smirnov, P. Kouminov, B. Voronov, N. Kaurova, V. Drakinsky, J. Zhang, A. Verevkin, and R. Sobolewski, "Fabrication of nanostructured superconducting single-photon detectors," *IEEE Trans. Appl. Superconduct.*, vol. 13, no. 2, pp. 192–195, Jun. 2003.

[20] B. Abdo, E. Segev, O. Shtempluck, and E. Buks, "Observation of Bifurcations and Hysteresis in Nonlinear NbN Superconducting Microwave Resonators," *cond-mat/0501114 v2*, 2005.

[21] B. Delaeta, J.-C. Villegierb, W. Escoffierb, J.-L. Thomassinb, P. Feautriera, I. Wangc, P. Renaud-Goudc, and J.-P. Poizat, "Fabrication and characterization of ultra-thin NbN hot electron bolometer for near infrared single photon detection," *Nucl. Instr. Meth. A*, vol. 520, pp. 541–543, 2004.

[22] A. Lichtenberger, D. Lea, and F. Lloyd, "Investigation of etching techniques for superconducting Nb/Al$-Al_2O_3$/Nb fabrication processes," *IEEE Trans. Appl. Superconduct.*, vol. 3, no. 1, pp. 2191–2196, Mar. 1993.

[23] J. R. Mileham, S. J. Pearton, C. R. Abernathy, J. D. MacKenzie, R. J. Shul, and S. P. Kilcoyne, "Wet chemical etching of AlN," *Appl. Phys. Lett.*, vol. 67, no. 8, pp. 1119–1121, Aug. 1995.

[24] A. V. Gurevich and R. G. Mints, "Self-heating in normal metals and superconductors," *Rev. Mod. Phys.*, vol. 59, no. 4, pp. 941–999, Oct. 1987.

[25] J. Zhang, W. Slysz, A. Pearlman, A. Verevkin, R. Sobolewski, O. Okunev, G. Chulkova, and G. N. Goltsman, "Time delay of resistive-state formation in superconducting stripes excited by single optical photons," *Phys. Rev. B*, vol. 67, no. 132508, 2003.

[26] B. Abdo, E. Segev, O. Shtempluck, and E. Buks, "Nonlinear Dynamics in the Resonance Lineshape of NbN Superconducting Resonators," *Phys. Rev. B*, vol. 73, no. 134513, 2006.

[27] P. Gardner, D. K. Paul, and K. P. Tan, "Planar microstrip ring resonator filters," in *IEE Colloquium Antennas for Personal Communication Systems*, Feb. 1994, pp. 6/1–6/6.

[28] S. M. Anlage, H. J. Snortland, and M. R. Beasley, "A current controlled variable delay superconducting transmission line," *IEEE Trans. Magn.*, vol. 25, no. 2, pp. 1388–1391, Mar. 1989.

[29] S. Cho, J.-C. Park, and C. Lee, "Current and temperature controlled variable inductance insuperconducting microstrip lines," *IEEE Trans. Appl. Superconduct.*, vol. 11, no. 1, pp. 3090–3093, Mar. 2001.

[30] R. E. Collin, *Foundations for Microwave Engineering*, 2nd ed. New York: McGraw-Hill, 1992, pp. 538–541.

[31] A. H. Majedi, S. K. Chaudhuri, and S. Safavi-Naeini, "Optical-microwave interaction modeling in high-temperature superconducting films," *IEEE Trans. Microw. Theory Tech.*, vol. 49, no. 10, pp. 1873–1881, Oct. 2001.

[32] B. Abdo, E. Segev, O. Shtempluck, and E. Buks, "Intermodulation gain in nonlinear NbN superconducting microwave resonators," *Appl. Phys. Lett.*, vol. 88, no. 1, p. 022508, Jan. 2006.

[33] E. Arbel-Segev, B. Abdo, O. Shtempluck, and E. Buks, "Novel self-sustained modulations in superconducting resonators," , arXiv:cond-mat/0607259.

[34] R. Sobolewski, Y. Xu, X. Zheng, C. Williams, J. Zheng, A. Verevkin, G. Chulkova, A. Korneev, A. Lipatov, O. Okunev, K. Smirnov, and G. N. Gol'tsman, "Spectral sensitivity of the NbN single-photon superconducting detector," *IEICE Trans. Electron.*, vol. E85-C, pp. 797–802, Mar. 2002.

[35] A. Korneev, P. Kouminov, V. Matvienko, G. Chulkova, K. Smirnov, B. Voronov, G. N. Goltsman, M. Currie, W. Lo, K. Wilsher, J. Zhang, W. Slysz, A. Pearlman, A. Verevkin, and R. Sobolewskic, "Sensitivity and gigahertz counting performance of NbN superconducting single-photon detectors," *Appl. Phys. Lett.*, vol. 84, no. 26, pp. 5338–5340, Jun. 2004.

[36] B. Abdo, E. Segev, O. Shtempluck, and E. Buks, "Nonlinear Coupling in Nb/NbN Superconducting Microwave Resonators," *arXiv:cond-mat/0501236 v1*, Jan. 2005.